A Review of Swelling Effect on Shale Permeability: Assessments and Perspectives

Qi Gao, Jishan Liu,* Yee-Kwong Leong, and Derek Elsworth

Cite This: *Energy Fuels* 2023, 37, 3488−3500

Read Online

ACCESS | Metrics & More | Article Recommendations | Supporting Information

ABSTRACT: The significant effect of gas sorption induced swelling on shale permeability has been observed through laboratory measurements and explained through permeability models over the past decades. However, there are lab observations that cannot be explained by these models. This knowledge gap prompts this review. Our goal is to form perspectives on how to resolve this gap through assessing the role of swelling on shale permeability. This goal is achieved through the following three steps: (1) collection of experimental shale permeability data measured under both constant effective stress and constant confining pressure conditions; (2) collection and classification of shale permeability models under the influence of gas sorption induced swelling strains; (3) assessments of co-relations between shale permeability data and permeability models. On the basis of all assessments, we conclude that the discrepancies between model predictions and laboratory measurements depend on the relation between bulk and pore

swelling strains, pore size scales, and consistencies of strain treatments in the experiments and models. Models assuming that bulk swelling strain is different from pore swelling strain can better explain lab observations than those assuming that they are the same. When the pore size transitions from the micron-scale to the nano-scale, the effect of swelling on shale permeability gradually diminishes. The inconsistencies between how swelling strains are measured in the lab and treated in the models are common in the literatures and affect the discrepancies between model predictions and lab observations. On the basis of these assessments, we form our perspectives: (1) transformation between bulk and pore swelling strains should be characterized and incorporated both for experiments and in permeability models; (2) shale multiscale pore structural characteristics should be characterized when assessing the swelling effect on shale permeability; (3) the time-dependent nature of swelling strain and permeability evolution should be incorporated into future experiments and permeability models.
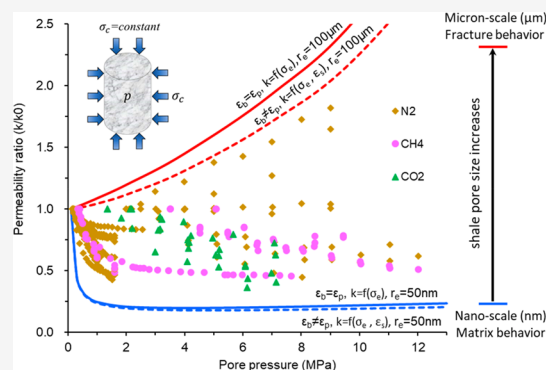
1. INTRODUCTION

As a typical type of multiporosity medium, shale consists of porous matrixes and natural fractures. Porous matrixes can be further divided into organic matter and inorganic matter. As nanopores inside the organic matter have extremely large internal surface area with strong affinity to methane, up to 20−85% of total shale gas initially in place could be adsorbed gas.[1−5] The production of this gas in place is strongly influenced by shale permeability. During the gas extraction process, reservoir pressure gradually declines, leading to an effective stress increase, rock compaction, and intrinsic permeability change. When reservoir pressure declines below the desorption point,[6] adsorbed gas starts to release, causing matrix shrinkage and further intrinsic permeability change.[7−9] Meanwhile, under the low pore pressure condition, gas slippage phenomenon occurs in the tiny nanopores. The occurrence of gas slippage will lead to apparent permeability change.[10−13] Therefore, shale permeability evolution is very complex and still has not been well understood.

Great efforts have been made in the laboratory to assess shale permeability evolution behaviors. These experiments are completed commonly under three different boundary conditions including the constant effective stress (CES) condition, constant pore pressure (CPP) condition, and constant confining pressure (CCP) condition. In CES tests, effective stress is kept constant. Shale permeability is believed to be influenced by gas sorption and gas slippage. In CPP tests, pore pressure is kept constant. Shale permeability is believed to be influenced by effective stress and gas slippage. In CCP tests, confining pressure is kept constant. Shale permeability is believed to be influenced by effective stress, gas sorption, and gas slippage. The basic assumption behind these tests is that the effects of effective stress, gas sorption, and gas slippage on shale permeability can be separated and studied individually.[14]
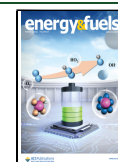
From the literatures, various CES tests have been done to investigate gas sorption on shale permeability,[15−20] to characterize the influence of gas slippage on shale permeability,[17−28] and to study the magnitude of effective stress on shale permeability.[21−24] Various CPP tests have been conducted to investigate the variation of effective stress and the role of gas slippage on shale permeability.[29−40] Various CCP tests have been completed to determine the individual effects of effective stress,[30,31,41,42] gas sorption,[30,31,41,42] and gas slippage[14,30,32,43−47] on shale permeability.

Although laboratory experiments are the most direct way to assess shale permeability behaviors, it is sometimes expensive, time-consuming, and even requiring massive manpower. To this end, numerous theoretical models have been developed. In this work, we divide the development of these theoretical shale permeability models into three stages. In the first stage, only gas slippage effect is considered. The effect of gas slippage can be incorporated into permeability models through two different methods. In the first method, the slip boundary condition of the continuity model is modified through multiplying a slippage factor to the continuity equation.[25,48−51] In the second method, various flow regimes are captured by permeability models through superposition of each flow regime using the contribution weight coefficients.[10,52−62] However, all permeability models in this stage assume intrinsic permeability as a constant, which is unrealistic during gas injection/extraction processes. In the second stage, the combined effects of effective stress and gas slippage are considered. These permeability models[14,63,64] are able to capture the deformation of shale and alteration of pore size as a result of effective stress change under variable boundary conditions spanning from displacement-controlled to stress-controlled ones. In the third stage, the combined effects of effective stress, gas sorption, and gas slippage are considered. In these permeability models, gas sorption affects shale permeability from two different aspects. On the one hand, the gas adsorption layer on nanopore wall reduces the effective radius of nanopores[65−69] and thus influences shale permeability. On the other hand, gas adsorption on rock grains causes matrix swelling, compresses the nanopore radius, and thus changes the shale permeability.[14,30,70−81] In addition to the above-mentioned three factors, shale permeability could also be influenced by other factors. For instance, Cai et al.[82] proposed an easy-to-implement model and disclosed that shale permeability could be influenced by heterogeneous pore size distribution. Sun et al.[83] pointed out that shale permeability could be influenced by shear deformation. The impacts of these factors are beyond the scope of this review and will not be further discussed.

In summary, both experimental and theoretical studies have been conducted to assess shale permeability evolution behaviors. The primary goal of this work is to assess how well the effect of gas sorption induced swelling on shale permeability has been considered in those permeability models. To achieve this goal, we first collect experimental shale permeability data that were measured under the CES and CCP conditions. Then, those shale permeability models that consider the effect of gas sorption induced swelling are collected and classified. Afterward, the co-relations between experimental shale permeability data and permeability models are assessed. In the end, the challenges on how to treat swelling strains in theoretical models and how to measure swelling strains in the laboratory are discussed and also future research directions are identified.

2. REVIEW OF EXPERIMENTAL SHALE PERMEABILITY DATA

A broad variety of experiments have been conducted in the laboratory to assess shale permeability evolution behaviors. Three typical boundary conditions are commonly used including the CES condition, CPP condition, and CCP condition. Under the CPP condition, swelling strain remains unchanged and does not influence shale permeability. Therefore, the focus of this section is on the review of experimental shale permeability data that were measured under the CES and CCP conditions.

2.1. Shale Permeability Data from CES Tests. In CES tests, effective stress is kept constant, which means that the difference between confining pressure and pore pressure is maintained unchanged throughout. Under this condition, gas sorption and gas slippage jointly control the evolution of shale permeability.

Figure 1 shows a variety of shale permeability data that were measured under the CES condition. In these tests, shale
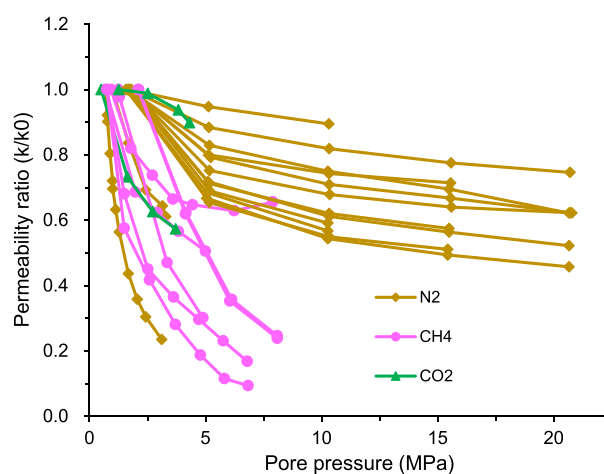

Figure 1. Distribution of shale permeability ratios that were measured under the CES condition.[15−20,22,23,45]

permeability was measured by either a steady state method or a pressure transient method. The detailed experimental procedures of these two methods will not be introduced in this paper. Readers who are interested in it are referred to our previous work.[84] In order to clearly show and compare how shale permeability evolves under the CES condition, the collected permeability data were normalized by using the permeability ratio (k/k_0), which is defined as the ratio of current permeability to initial permeability. As the gas pressure may either be increased or decreased during the permeability tests, in this review we use the change of permeability ratio from a lower pressure condition to that at a larger pressure condition to study shale permeability evolution behaviors.

As can be seen, shale permeability ratios distribute over a wide range with all values less than 1 and greater than 0.09. These permeability ratios are measured by using different adsorptive gas sources including N_2, CH_4, and CO_2. Among these gases, CO_2 has the strongest adsorption capacity, followed by CH_4 and then N_2.[85] In these CES tests, the magnitude of effective stress varies from 3.4 to 20.7 MPa and the magnitude of injection pressure varies from 0.5 to 20.7 MPa. It can be found that under the CES condition all shale permeability ratios decrease with the increase of gas pressure.

When CO_2 or CH_4 (strongly adsorptive gases) is used as the injection gas, the shale permeability ratio sharply decreases with the gas pressure increase. When N_2 (weakly adsorptive gas) is used as the injection gas, the shale permeability ratio changes within a wider range with the gas pressure increase. This finding suggests that shale permeability evolution is closely related to gas sorption. For further observation, shale permeability declines at different rates in those experiments that were conducted using the same gas source, which implies that shale permeability evolution also depends on other factors such as effective stress magnitude and pore structure inside the tested samples.

2.2. Shale Permeability Data from CCP Tests. In CCP tests, confining pressure remains constant while the effective stress gradually changes with gas pressure increase/decrease. Under this condition, gas sorption, effective stress, and gas slippage jointly control shale permeability evolution.

In this subsection, we use the permeability ratio (k/k_0) to analyze those data collected under the CCP condition as well. As can be seen from Figure 2, shale permeability ratios
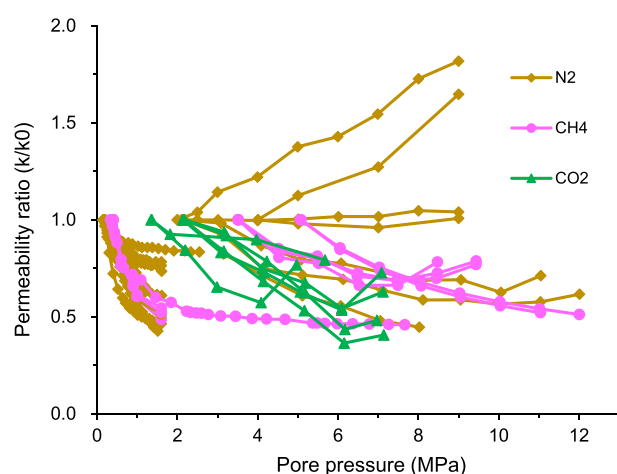

Figure 2. Distribution of shale permeability ratios that were measured under the CCP condition.[14,20,31,32,41−46]

distribute over a wide range from 0.35 to 1.8 under the CCP condition. Similar to the CES tests, these permeability ratios represent the measurements by the use of different adsorptive gas sources including N_2, CH_4, and CO_2. In these CCP tests, the magnitude of confining pressure varies from 7 to 31.8 MPa and the magnitude of injection pressure varies from 0.15 to 12 MPa. It can be found that shale permeability evolution behaviors can be classified into three categories: permeability continuously increases with gas pressure increase; permeability initially decreases and then rebounds with gas pressure increase; permeability continuously decreases with gas pressure increase. If we use $k/k_0 = 1$ as the baseline, these permeability ratios can be divided into the upper part and the lower part, respectively representing the permeability net-increasing zone and net-decreasing zone. When CO_2 or CH_4 (strongly adsorptive gases) is used as the injection gas, shale permeability ratios are mainly confined within the net-decreasing zone. When N_2 (weakly adsorptive gas) is used as the injection gas, shale permeability ratios distribute widely throughout the net-increasing and net-decreasing zones. This observation suggests that shale permeability change is closely related to gas sorption. For further observation, shale

permeability evolution behaviors can be distinctively different from each other in those experiments where the same gas source is used. This implies that the magnitude of confining pressure and the internal pore structure characteristics of the tested samples could also be important influencing factors.

3. REVIEW OF SHALE PERMEABILITY MODELS

In this section, the individual effects of gas sorption, effective stress, and gas slippage on shale permeability evolution are first analyzed. Then, shale permeability models that consider the combined effects of the three competing mechanisms are collected and classified. The model classification is based on how swelling strains are handled in the derivation process of these shale permeability models.

3.1. Competing Mechanisms in Shale Permeability Evolution. During adsorptive gas injection/extraction, shale permeability will be altered under the combined effects of effective stress, gas sorption, and gas slippage. The effective stress change and gas sorption induced swelling jointly alter the intrinsic permeability, while gas slippage alters the apparent permeability. In this subsection, how shale deforms and permeability evolves during adsorptive gas injection under the CES and CCP conditions are analyzed.

Figure 3a shows the initial state of a representative elementary volume (REV) that has an idealized pore locating
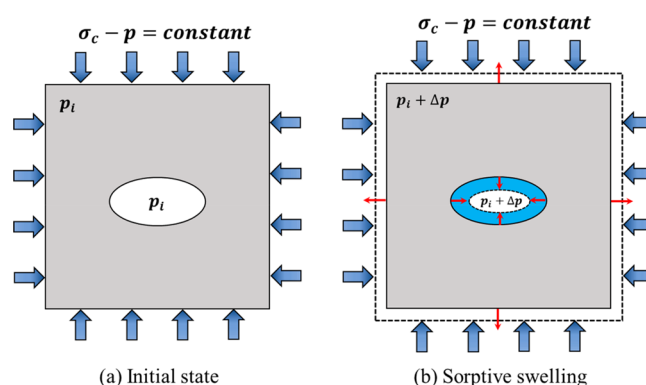

(a) Initial state   (b) Sorptive swelling

Figure 3. Shale deformation during adsorptive gas injection under the CES condition.

at the center of the shale matrix. When gas pressure in this REV increases under the CES condition, only gas sorption induced swelling contributes to shale deformation. As shown in Figure 3b, the matrix externally swells when gas adsorbs on shale grains but the pore inside the matrix is internally compressed. When the gas pressure in the REV increases under the CCP condition, both the effective stress change and gas sorption induced swelling contribute to shale deformation. As shown in Figure 4b,c, both the matrix and pore expand due to effective stress decline while the matrix expands and the pore closes due to swelling. Thus, under the CCP condition, increasing the pore pressure in shale with an adsorptive gas causes the pore size to increase due to poromechanical expansion and meanwhile to decrease due to gas sorption induced swelling. When the gas pressure is greater than the equilibrium pressure, effective stress decline induced pore expansion outcompetes swelling induced pore closure.[7] In addition, gas slippage plays a critical role in altering the shale permeability especially under the low pore pressure condition and in tiny nanopores.[86−88] The individual contributions of the
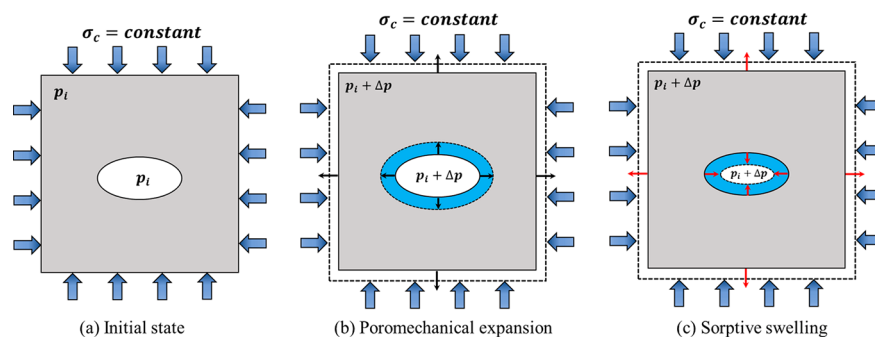
Figure 4. Shale deformation during adsorptive gas injection under the CCP condition.
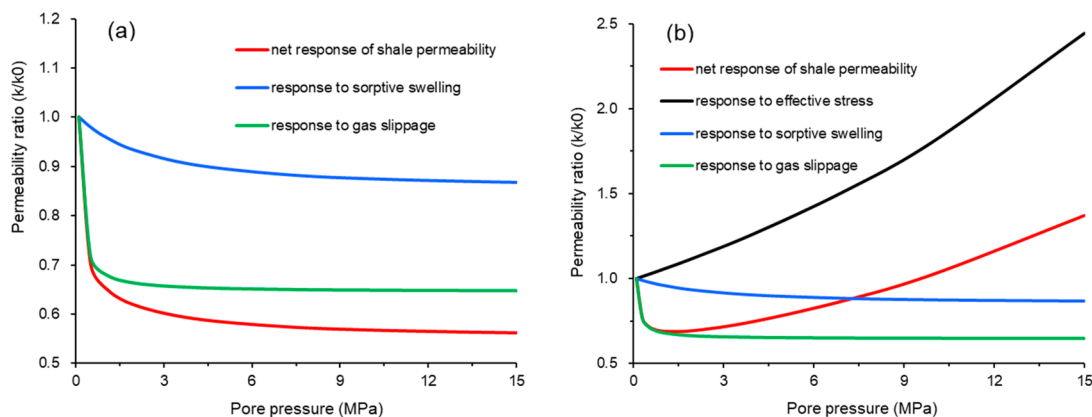

Figure 5. Shale permeability evolution under different boundary conditions: (a) CES condition; (b) CCP condition.

three competing mechanisms to shale permeability evolution are depicted in Figure 5. Note that the magnitude and variation trend of these curves could be changed when different pore sizes, pore compressibilities, and Langmuir parameters are used.

3.2. Collection and Classification of Shale Permeability Models. Numerous theoretical models have been developed to characterize the evolution behaviors of shale permeability. A vast majority of these models focus on investigating the effect of gas slippage on shale permeability. However, there is a common assumption behind these models that no stress change and solid deformation occur in the rock, which is unrealistic under both field and laboratory conditions. In order to better explain shale permeability evolution, permeability models are improved to incorporate the effects of effective stress and gas sorption. The inclusion of effective stress, gas sorption, and gas slippage in theoretical models makes shale permeability prediction results more reliable. In this subsection, these improved shale permeability models are collected and then classified.

Table 1 summarizes shale permeability models that consider the combined effects of the three competing mechanisms. These models can be classified into two major categories according to how the swelling term is handled in the derivation process of these models. In the first category, gas sorption induced bulk swelling strain is assumed to be identical to pore swelling strain. With this assumption, under variable stress conditions, bulk swelling strain and pore swelling strain cancel each other out and shale intrinsic permeability is defined as a function of the effective stress or effective strain. Based on the models in this category, gas sorption induced matrix swelling or shrinkage will not contribute to shale intrinsic permeability

change under the CES condition. However, this conclusion contradicts with the collected shale permeability data from the CES tests. From Figure 1, it can be known that the shale intrinsic permeability still continues to decline rather than remaining unchanged when the gas slippage effect disappears (normally when the pore pressure is greater than 5 MPa), which implies that gas sorption induced swelling indeed will influence shale intrinsic permeability under the CES condition. The contradiction between laboratory observations and model prediction requires the removal of the assumption that bulk and pore swelling strains are identical when studying the impact of swelling on shale permeability change.

In the second category, a more general form of shale intrinsic permeability model is developed by assuming that bulk swelling strain and pore swelling strain have different magnitudes. With this assumption, under variable stress conditions, shale intrinsic permeability is defined as a function of effective stress, bulk/pore swelling strain, and the strain splitting factor. The strain splitting factor defines the relation between pore and bulk swelling strains.

As permeability models in these two categories are expressed in various forms, it is inconvenient to make a direct comparison between these models. To this end, a generic shale permeability model is developed which can be degenerated into the permeability models in both category one and category two. The detailed derivation process of this generic shale permeability model is given in the Supporting Information. When bulk and pore swelling strains are assumed to be the same, the generic shale permeability model is degenerated into the model that can represent shale permeability models in category one:

Table 1. Summary of Shale Permeability Models That Consider the Combined Effects of Gas Sorption, Effective Stress, and Gas Slippage

model source	expression	notes	category
	Category One		
Pan et al.[30]	$\dfrac{k}{k_0} = e^{-3c_f(\bar{\sigma}-\bar{\sigma}_0)}\left(1 + \dfrac{b}{P_b}\right)$	b is Klinkenberg constant	category one: bulk and pore swelling strains are assumed to be identical
Cao et al.[70]	$\dfrac{k}{k_0} = \exp\{-3c_f[(\bar{\sigma}-\bar{\sigma}_0)-(p-p_0)]\}(1+\zeta Kn)\left(1+\dfrac{4Kn}{1+Kn}\right)$	Kn is Knudsen number	
Wei et al.[71]	$\dfrac{k}{k_0} = \left(1+\dfrac{\alpha}{\phi_0}\Delta\varepsilon_e\right)^3(1+\zeta Kn)\left(1+\dfrac{4Kn}{1+Kn}\right)$ $\Delta\varepsilon_e = \Delta\varepsilon_v + \dfrac{\Delta p}{K_s} - \Delta\varepsilon_s = -\dfrac{\Delta\bar{\sigma}-\Delta p}{K}$	ε_e is effective strain	
Gao et al.[8]	$k_{or} = w_{vs}k_{vs} + w_{kd}k_{kd} + k_{sf}$ $k_{vs} = \dfrac{1}{1+Kn/2}\dfrac{r_{or}^2}{8}(1+\alpha Kn)\left(1+\dfrac{4Kn}{1-bKn}\right)$ $r_{or} = r_{ori}\exp\left(-\dfrac{c_{ort}}{2}[(\bar{\sigma}_{or}-\bar{\sigma}_{ori})-(p_{or}-p_{ori})]\right)$	different flow regimes are considered; w_{vs} and w_{kd} are weighting coefficients for different flow regimes	
Wang et al.[72]	$k = w_v k_v + w_k k_k$ $\dfrac{k_v}{k_{v0}} = \exp\left\{-3c_f\left[-\dfrac{v}{1-v}(p-p_0)+\dfrac{E(1+v)}{3(1-v)}\Delta\varepsilon_s\right]\right\}, \quad$ in situ condition hydration stress condition $\dfrac{k_v}{k_{v0}} = \exp\left\{-3c_f\left[-(p-p_0)+\dfrac{E}{3(1-2v)}\Delta\varepsilon_s\right]\right\}$	different flow regimes are considered; w_v and w_k are weighting coefficients for different flow regimes	
Shi et al.[73]	$\dfrac{k}{k_0} = \left(1-\dfrac{\alpha}{\phi_0}\dfrac{\Delta\bar{\sigma}-\Delta p}{K}\right)^3\left(1+\dfrac{2\sqrt{2}ck_BT}{\pi\delta^2 p r_e}\right)$	k_B is Boltzmann constant; r_e is effective pore radius	
	Category Two		
Peng et al.[74]	$\dfrac{k}{k_0} = e^{-3c_f\Delta(\bar{\sigma}-p)-3C\Delta\varepsilon_s}(1+\zeta Kn)\left(1+\dfrac{4Kn}{1+Kn}\right)$ $\dfrac{k}{k_0} = \exp\left\{3c_f K\left(\Delta\varepsilon_v+\dfrac{\Delta p}{K_s}-\Delta\varepsilon_s\right)\left(1+\dfrac{4Kn}{1+Kn}\right)(1+\zeta Kn)-3C\Delta\varepsilon_s\right\}$	C is strain splitting factor	category two: bulk and pore swelling strains are assumed to have different magnitudes
Yang et al.[75]	$k = w_{bu}k_{co}(1+\zeta Kn)\left(1+\dfrac{4Kn}{1+Kn}\right) + w_{ad}\dfrac{\mu}{\rho_g}\dfrac{\phi}{\tau_h}M_g C_{admax}D_{ad0}\dfrac{1}{p+P_L}$ $k_{co} = k_{co0}\left\{\dfrac{1}{1+\varepsilon_{e0}+(1-\eta)\varepsilon_s}\left[1+\varepsilon_{e0}+(1-\eta)\varepsilon_{s0}+\dfrac{\alpha(\varepsilon_e-\varepsilon_{e0})}{\phi_0}\right]\right\}^3$	η is strain splitting factor; w_{bu} and w_{ad} are weighting coefficients for different flow regimes	
Li et al.[77]	$k = k_{intrinsic}k_{slippage}$	f is strain splitting factor; fractal characteristic of nanopores is considered	

Table 1. continued

model source	expression	notes	category
			Category Two
Li et al.[78]	$k_{\text{intrinsic}} = A(\varsigma)\dfrac{hL_0^{1-D_T}}{12A}\dfrac{D_f}{2+D_T-D_f}b_{\text{eff,max}}^{2+D_T}$ $b_{\text{eff}} = b_0\left[\exp(-c_f\Delta\sigma_e) - \dfrac{1}{b_0}f\dfrac{\Delta\epsilon_s}{3}\right]$	f is strain splitting factor; w_s and w_k are weighting coefficients for different flow regimes	
Gao et al.[79]	$k = w_s k_{co}(1 + 4Kn) + w_k k_{d} + k_f$ $k_{co} = k_{co0}\exp\{-3c_f[(\bar{\sigma}-\bar{\sigma}_0)-(p-p_0)] + 3(f-1)\Delta\epsilon_s^b\}$ $k_f = k_{f\text{-vs}} + k_{f\text{-kd}} + k_{f\text{-sf}}$ $k_{f\text{-vs}} = f(w),\ k_{f\text{-kd}} = f(w),\ k_{f\text{-sf}} = f(w)$ $w = w_0\exp\left(-\dfrac{\Delta\sigma_e}{Kn}\right) - f\cdot 2t_0\dfrac{\Delta\epsilon_s}{3} - 2d_m\theta$	f is strain splitting factor; w is microfracture aperture; different flow regimes are considered	
Zeng et al.[80]	$k_t = k_{vs} + k_k + k_{\text{surface}}$ $k_{vs} = f(b+\Delta b_t),\ k_k = f(b+\Delta b_t)$ $\Delta b_t = b_0 c_f\Delta\sigma_e + \dfrac{a_0(1-2v)}{E}(p-p_0) - \dfrac{a_0\epsilon_L P_L}{(P_L+p_0)(P_L+p)}(p-p_0)$	b is microfracture aperture; different flow regimes are considered	

$$k_{ap} = k_{in0} \exp\{-3c_p[(\overline{\sigma} - \overline{\sigma}_0) - (p - p_0)]\}$$
$$\left(1 + \frac{2\sqrt{2}\,ck_BT}{\pi\delta^2 p r_e}\right) \tag{1}$$

where k_{ap} is the shale apparent permeability, k_{in0} is the shale intrinsic permeability, c_p is the pore compressibility, $\overline{\sigma}$ is the mean compressive stress, p is the pore pressure, c is a proportionality factor, k_B is the Boltzmann constant, T is temperature, δ is the gas molecule diameter, and r_e is the pore radius.

When the bulk and pore swelling strains are assumed to have different magnitudes, the generic shale permeability model is degenerated into the model that can represent shale permeability models in category two:

$$k_{ap} = k_{in0} \exp\{-3c_p[(\overline{\sigma} - \overline{\sigma}_0) - (p - p_0)]$$
$$+ 3(f - 1)\Delta\varepsilon_s^b\}\left(1 + \frac{2\sqrt{2}\,ck_BT}{\pi\delta^2 p r_e}\right) \tag{2}$$

where $f = \frac{\Delta\varepsilon_s^p}{\Delta\varepsilon_s^b}$ is the strain splitting factor which defines the relation between bulk and pore swelling strains, and ε_s^b and ε_s^p represent bulk and pore swelling strains, respectively.

4. ANALYSIS OF SHALE PERMEABILITY DATA

In this section, the classified shale permeability models are used to explain the laboratory observations that shale permeability ratios distribute over a wide range under the CES and CCP conditions. This attempt provides significant insights into how shale permeability evolves under the combined effects of gas sorption, effective stress, and gas slippage and how the swelling term should be handled in shale permeability models.

4.1. Analysis of Shale Permeability Data under CES Condition. The distribution of experimental data and solutions of permeability models under the CES condition is shown in Figure 6. In Figure 6, the solid lines denote the solutions of eq 1, which represents the permeability models with identical swelling strains, while the dashed lines denote the solutions of eq 2, which represents the permeability models with nonidentical swelling strains. The input parameters for permeability calculation are summarized in Table 2.

As can be seen from Figure 6, the widely distributed shale permeability ratios are confined within the upper and lower boundaries. The upper boundary represents the permeability evolution behavior of fractured shale. In this case, shale permeability evolution is dominated by gas sorption while the effect of gas slippage can be ignored. The lower boundary represents the permeability evolution behavior of unfractured shale or shale matrix. In this case, the effect of gas slippage on shale permeability evolution is significant under the low pore pressure condition. Thus, the transition from the upper boundary to the lower boundary represents the evolution of shale pore size from the micron-scale to the nano-scale. It should be noted here that in this work we assume that fractured shale permeability is only contributed by fractures while the contribution from shale matrix is ignored. This is mainly because fracture permeability is commonly several orders of magnitude larger than matrix permeability.

Comparison between solid lines and dashed lines in Figure 6 indicates that the magnitude of shale permeability calculated
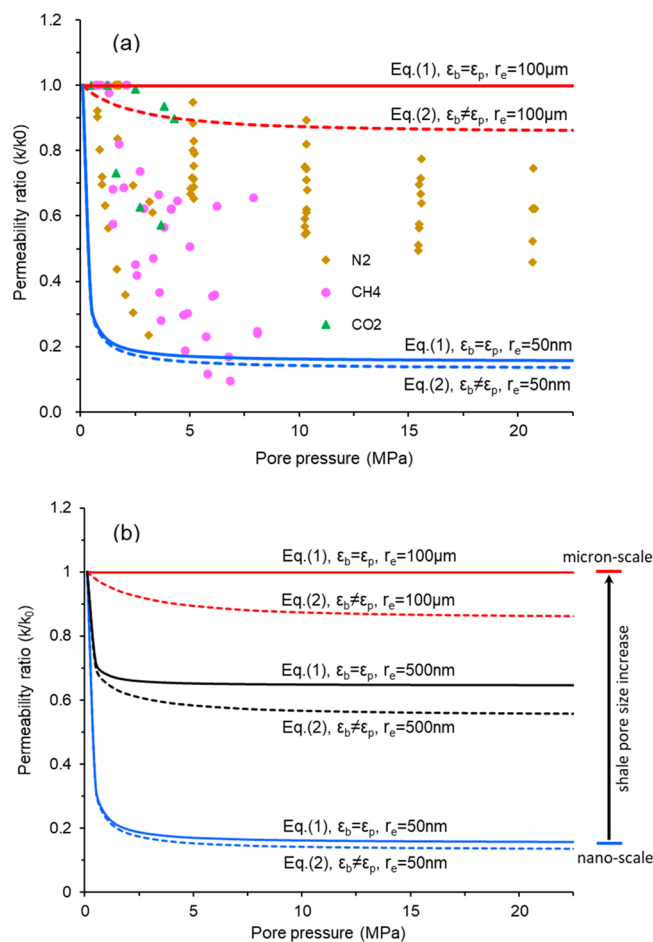
Figure 6. (a) Comparison between laboratory observation and theoretical solutions under the CES condition. (b) Theoretical solutions derived under different shale pore sizes.

Table 2. Input Parameters for Permeability Calculation[a]

parameter	value		
permeability curve color	red	black	blue
pore radius (m)	1×10^{-4}	5×10^{-7}	5×10^{-8}
compressibility (1/MPa)	0.03	0.02	0.01
Langmuir strain of shale bulk	0.005	0.005	0.005
Langmuir pressure of shale bulk (MPa)	7	7	7
Langmuir strain of shale matrix	0.009	0.009	0.009
Langmuir pressure of shale matrix (MPa)	4	4	4
temperature (K)	320	320	320
Boltzmann constant (J/K)	1.38×10^{-23}	1.38×10^{-23}	1.38×10^{-23}
gas molecule diameter (nm)	0.38	0.38	0.38

[a]Note that Langmuir parameters will not be used when calculating shale permeability using eq 1.

by eq 2 is lower than that calculated by eq 1 and that the solutions of eq 2 can better serve as the limiting boundaries of the experimental shale permeability data. This is because pore swelling strain and bulk swelling strain cancel each other out in the derivation process of eq 1 and thus, under the CES

condition, eq 1 is only able to disclose the effect of gas slippage on shale permeability and fails to include the effect of gas sorption. By contrast, eq 2 captures the effects of both gas slippage and gas sorption on shale permeability evolution as it is derived under the assumption that pore and bulk swelling strains have different magnitudes. It should be noted that there are still some permeability data lying outside the zone confined by the upper (red dashed line) and lower (blue dashed line) boundaries (Figure 6). This is mainly because the initial pressure applied in these tests is much larger than that used in our calculation. If a larger initial pressure is used in our calculation, these permeability data would be included in the limiting boundaries. In addition, it can be found that the difference between solid and dashed lines gradually diminishes when the shale pore size transitions from the micron-scale to the nano-scale, which implies that fracture permeability is more sensitive to gas sorption induced swelling than matrix permeability. This is mainly because the gas slippage effect is negligible in a fracture system and thus gas sorption plays the dominant role in controlling fracture permeability. However, in shale matrix, the gas slippage effect is much more pronounced and thus the effect of gas sorption induced swelling on matrix permeability is not that significant.

4.2. Analysis of Shale Permeability Data under CCP Condition. The distribution of experimental data and solutions of permeability models under the CCP condition is shown in Figure 7. In Figure 7, the solid lines denote the solutions of eq 1, which represents the permeability models with identical swelling strains, while the dashed lines denote the solutions of eq 2, which represents the permeability models with nonidentical swelling strains. The input parameters for permeability calculation are given in Table 2.

It can be observed that the distribution of shale permeability ratios is also confined within the upper and lower boundaries, which represent the permeability evolution behavior of fractured shale and unfractured shale (or shale matrix), respectively. Unlike the data from the CES tests, permeability data from the CCP tests are controlled by three competing mechanisms including effective stress, gas sorption, and gas slippage. For fractured shale, the effect of gas slippage on shale permeability can be neglected. Shale permeability evolves under the competing effects of effective stress and gas sorption. For unfractured shale or shale matrix, the gas slippage effect is pronounced under the low pore pressure condition. With pore pressure increasing, the effects of gas slippage and gas sorption on shale permeability are weakened and effective stress gradually plays the dominant role. In addition, it can be found that when shale permeability is dominated by effective stress, the increasing trend of fractured shale permeability is more obvious than that of unfractured shale permeability as the compressibility of fracture is larger than that of a nanopore.

Comparison between solid lines and dashed lines in Figure 7 also indicates that shale permeability values calculated by eq 2 are lower than those calculated by eq 1 and that the solutions of eq 2 can better serve as the limiting boundaries of the widely distributed shale permeability data. For further observation, the difference between solid and dashed lines is narrowed when shale pore size transitions from the micron-scale to the nano-scale, which implies that fracture permeability is more sensitive to gas sorption induced swelling than matrix permeability.
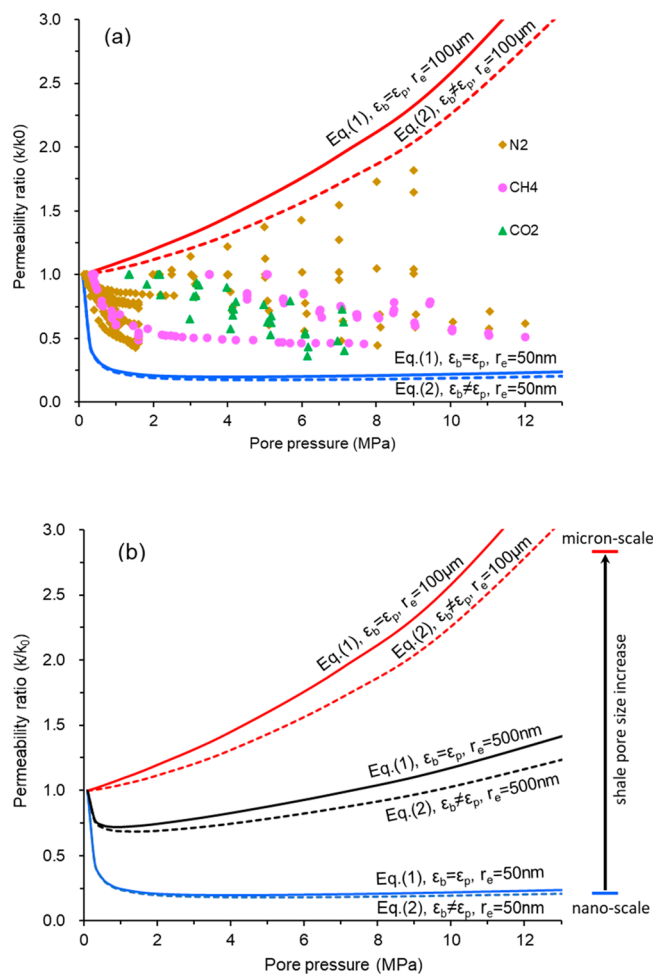

Figure 7. (a) Comparison between laboratory observation and theoretical solutions under the CCP condition. (b) Theoretical solutions derived under different shale pore sizes.

5. CHALLENGES AND PERSPECTIVES

Although the effect of swelling on shale permeability evolution has been assessed through both theoretical and experimental studies, some critical issues are still not resolved. The focus of this section is on the discussion of these issues and then identifying the potential areas for future research.

From the perspective of theoretical study, modeling shale permeability evolution at either the core scale or reservoir scale requires the establishment of a set of partial differential equations to define the involved coupled hydromechanical processes: (1) geomechanical deformation of shale and (2) fluid flow in shale. The commonly used equations to define these two processes are given as eqs 3 and 4:[70,89−92]

$$Gu_{i,kk} + \frac{G}{1-2\nu}u_{k,ki} - \alpha p_i - K\varepsilon^{b}_{s,i} + f_i = 0 \tag{3}$$

$$\frac{\partial\left(\rho_g\phi + \rho_{ga}\rho_s\frac{V^{b}_{L}p}{p+P^{b}_{L}}\right)}{\partial t} + \nabla\cdot\left(-\rho_g\frac{k_{ap}}{\mu_g}\nabla p\right) = 0 \tag{4}$$

where G is the shear modulus, ν is Poisson's ratio, α is the Biot coefficient, K is the bulk modulus, u_i is the component of displacement, f_i is the component of body force, ρ_g is the gas density, ρ_{ga} is the gas density at standard conditions, ρ_s is the shale density, μ_g is the gas viscosity, V^{b}_{L} is the Langmuir volume

of shale bulk, and P_L^b is the Langmuir pressure of shale bulk. In eq 3, a comma followed by a subscript represents the differentiation with respect to spatial coordinates and repeated indices in the same equation denote summation over the range of the indices.

Shale geomechanical deformation and fluid flow processes have been defined by eqs 3 and 4, respectively. The interactions of these two processes can be linked through shale porosity and permeability models:[93−96,105]

$$\frac{\phi}{\phi_0} = \exp\{-c_p[(\sigma - \sigma_0) - (p - p_0)] + (f - 1)\Delta\varepsilon_s^b\}$$

(5)

$$\frac{k_{ap}}{k_{in0}} = \exp\{-3c_p[(\overline{\sigma} - \overline{\sigma}_0) - (p - p_0)] + 3(f - 1)\Delta\varepsilon_s^b\}$$

$$\left(1 + \frac{2\sqrt{2}\,ck_BT}{\pi\delta^2 p r_e}\right)$$

(6)

From eqs 3−6, it can be known that gas sorption plays important roles in the gas injection (or extraction) process in shale. Specifically, gas adsorption on shale grains will induce shale swelling. The swelling effect on shale mechanical deformation is defined in the fourth term of eq 3, i.e., $K\varepsilon_{s,i}^b$. When shale swells, the pore size will be altered and the permeability will be changed. The second term in eqs 5 and 6, i.e., $(f - 1)\Delta\varepsilon_s^b$, defines the effect of gas sorption induced swelling on shale porosity and permeability change. The change of porosity and permeability will further influence the gas flow and pore pressure distribution in shale. Subsequently, the change in pore pressure will influence the effective stress and shale mechanical deformation. Thus, it can be concluded that shale deformation, gas flow, and porosity and permeability changes will all be influenced by gas sorption. It is widely accepted that the swelling term ε_s^b in eqs 3, 5, and 6 can be defined in the form of[97,98]

$$\varepsilon_s^b = \frac{\varepsilon_L^b p}{p + P_L^b}$$

(7)

where ε_L^b is the Langmuir strain of shale bulk and P_L^b is the Langmuir pressure of shale bulk. Both Langmuir strain and Langmuir pressure can be obtained through fitting the laboratory measured swelling strain into the Langmuir-type curve.[7,97−99] On the fitted curve, the strain at infinite pressure represents Langmuir strain and the pressure at which the measured strain is half of its maximum value represents Langmuir pressure.

In the current stage, there still remains inconsistency among the stress equilibrium equation, i.e., eq 3, porosity/permeability models, i.e., eqs 5 and 6, and laboratory measurements with respect to how swelling strains are handled. In the stress equilibrium equation and porosity/permeability models, the bulk swelling strain represents the volumetric strain of shale that is purely induced by gas adsorption. However, in the laboratory, the bulk swelling strain is commonly measured under the hydrostatic stress condition, as shown in Figure 8. During the experiment, adsorptive gas is injected into the high-pressure chamber until the anticipated pressure is reached. Then, the bulk swelling strain of shale sample is directly measured by the attached strain gauges when gas pressure inside the chamber is stabilized.[15,100,101] The measured bulk swelling strain actually consists of two components. One
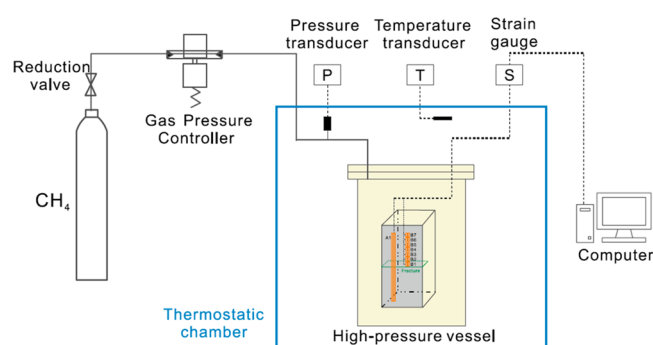

Figure 8. Schematic diagram of how swelling strain is measured in laboratory. [Reproduced with permission from ref 101. Copyright 2020 Elsevier.]

component is the swelling strain purely induced by gas adsorption. The other component is the compressive strain induced by hydrostatic pressure. Therefore, directly inputting the laboratory measured strain and fitted Langmuir parameters into the stress equilibrium equation and porosity/permeability models will theoretically underestimate the impact of gas sorption induced swelling on shale deformation and porosity/permeability change. In order to keep the consistency between laboratory measured strains and the model-used ones, compressive strain caused by hydrostatic pressure should be subtracted from the measured bulk strain.

According to eqs 5 and 6, shale porosity and permeability are defined as a function of pore and bulk swelling strains. The popular viewpoint now is that bulk and pore swelling strains are either the same[8,30,70−73] or have different magnitudes.[74−79,102−104] Our analysis in section 3.2 indicates that bulk and pore swelling strains should have different magnitudes rather than being the same. When bulk and pore swelling strains are assumed to have different magnitudes, a constant ratio, namely the strain splitting factor, has been widely used to define the relation between these two strains. In this way, shale porosity/permeability models can only represent the role of either bulk or pore swelling strain and fail to characterize the real relation between them. Thus, these efforts to distinguish bulk and pore swelling strains still remain questionable. In fact, bulk and pore swelling strains are interdependent and can be transformed from each other. This strain transformation is very complex and could be influenced by various factors such as shale microstructure, total organic carbon (TOC) content, mechanical boundary conditions, etc. In the future, new theoretical approaches should be developed to characterize the real relation between them under different conditions. Then, this characterization should be incorporated into shale permeability models to explain the lab/field observations. Furthermore, to the best of the authors' knowledge, almost all experimental studies in the current stage focus on measuring the bulk swelling strain and pore swelling strain measurement is still rarely reported. Therefore, novel experimental methods should be designed to simultaneously measure bulk and pore swelling strains, which can then be used to validate the theoretical relations between them.

Comparison between theoretical solutions and permeability data in Figures 6 and 7 indicates that permeability evolution behaviors of fractured shale and unfractured shale define the upper and lower boundaries, respectively. For actual shales with self-contained multiscale pore structures, permeability evolution should be confined in-between. As gas sorption

induced swelling impacts shale permeability in varying degrees at different pore scales, the swelling effect on shale permeability cannot be fully understood without the knowledge of multiscale pore structural characteristics. In the future, shale multiscale pore structural characteristics should be first characterized using the experimental methods and then incorporated into shale permeability models when assessing the swelling effect on permeability evolution.

It should be noted that all the above analysis and discussion are based on a common assumption that the ultimate equilibrium state has been reached in shale; i.e., gas pressures in fracture and solid matrix systems are equilibrated. This assumption maybe applicable for unfractured shale or shale matrix, but it does not work for fractured shale. In fractured shale, there exists a huge contrast between fracture and matrix permeabilities. Due to this naturally huge permeability contrast, it may take several months or even a few years for shale to reach the ultimate equilibrium state as gas diffusion from the fracture wall into the shale matrix is a very slow process. This transient process will induce a nonuniform pore pressure distribution in the shale matrix, and thus the induced swelling strain is time-dependent and nonuniform as well.[89,100] Under this condition, shale permeability evolution behaviors become much more complex and cannot be explained by the models as summarized in Table 2. Thus, current experimental and theoretical approaches should be redesigned to capture the time-dependent behaviors of swelling strain and permeability evolution in fractured shale.

6. CONCLUSIONS

Various experimental and theoretical studies of gas sorption induced swelling effect on shale permeability evolution behaviors have been reviewed. Based on the results of the review, the following conclusions can be drawn:

1. Permeability models with nonidentical swelling strains can define the swelling effect better than those with identical swelling strains. When swelling strains are assumed to be identical, shale intrinsic permeability is defined as a function of effective stress. When swelling strains are assumed to be nonidentical, shale intrinsic permeability can be defined as a function of both effective stress and swelling strain. Comparison between experimental data and solutions of these permeability models indicates that permeability models with nonidentical swelling strains can better explain the laboratory observations.

2. The effect of gas sorption induced swelling on shale permeability is pore size dependent. When shale pore size transitions from the micron-scale to the nano-scale, the difference between the solutions of the permeability models with identical swelling strains and those with nonidentical swelling strains gradually diminishes. This means that fractured shale permeability is more sensitive to gas sorption induced swelling than unfractured shale or shale matrix permeability.

3. The inconsistency between how swelling strains measured in the laboratory and treated in the models affects the characterization of swelling effect. In the laboratory, the measured bulk swelling strain typically consists of two components including gas adsorption induced swelling strain and hydrostatic pressure induced compression strain. In theoretical models, the bulk swelling strain represents the volumetric strain purely induced by gas adsorption. Thus, directly inputting the measured swelling strain into theoretical models will underestimate the swelling effect.

■ ASSOCIATED CONTENT

ⓢ Supporting Information

The Supporting Information is available free of charge at https://pubs.acs.org/doi/10.1021/acs.energyfuels.2c04005.

Derivation process of the generic shale permeability model (PDF)

■ AUTHOR INFORMATION

Corresponding Author

Jishan Liu − School of Engineering, The University of Western Australia, Perth, Western Australia 6009, Australia; ⓘ orcid.org/0000-0002-2744-0319; Email: jishan.liu@uwa.edu.au

Authors

Qi Gao − School of Engineering, The University of Western Australia, Perth, Western Australia 6009, Australia

Yee-Kwong Leong − School of Engineering, The University of Western Australia, Perth, Western Australia 6009, Australia

Derek Elsworth − Department of Energy and Mineral Engineering, G3 Centre and Energy Institute, The Pennsylvania State University, University Park, Pennsylvania 16802, United States

Complete contact information is available at:
https://pubs.acs.org/10.1021/acs.energyfuels.2c04005

Notes

The authors declare no competing financial interest.

Biographies

Qi Gao received his B.Eng. and M.Eng. degrees in petroleum engineering from China University of Petroleum (East China) in 2016 and 2019, respectively. He is currently a Ph.D. student at The University of Western Australia. Qi's research interests are in the areas of unconventional reservoir geomechanics and geo-multiphysics with application to shale gas and coalbed methane extraction.

Jishan Liu is a professor in the School of Engineering, The University of Western Australia. Jishan received his Ph.D. degree in mining engineering from The Pennsylvania State University in 1996. Since then, he has been working primarily at The University of Western Australia. His research interests cover unconventional reservoir multiphysics (URM) with application to coal seam gas extraction, shale gas extraction, stacked deposits extraction, CO_2 sequestration, coal mine safety, and caprock sealing safety.

Yee-Kwong Leong is a professor in the School of Engineering, The University of Western Australia. He received his Ph.D. degree in chemical engineering from the University of Melbourne in 1989. His research interests mainly include surface chemistry, microstructure, and rheology of clay and oxide suspensions; surface forces and microstructure of thixotropic clay suspensions; coal and biochar slurry fuel preparation; inverse problems in viscometery; and chemical kinetics and thermodynamics.

Derek Elsworth is G. Albert Shoemaker Chair and Professor of Energy and Mineral Engineering and Geosciences at The Pennsylvania State University. He is cofounder of the Center for Geomechanics, Geofluids, and Geohazards. His interests are in the areas of computational mechanics and rock mechanics and in the mechanical and transport characteristics of fractured rocks, with application to geothermal energy, the deep geological sequestration of radioactive wastes and of CO_2, unconventional hydrocarbons including coal gas, tight gas shales, and hydrates, and the instability and eruption dynamics of volcanoes.

■ ACKNOWLEDGMENTS

■ REFERENCES

(1) Darishchev, A.; de Nancy, E. N.; Lemouzy, P.; Rouvroy, P. On simulation of flow in tight and shale gas reservoirs. Presented at the SPE Unconventional Gas Conference and Exhibition, Muscat, Oman, 2013.

(2) Wang, H. Y.; Ajao, O.; Economides, M. J. Conceptual study of thermal stimulation in shale gas formations. *J. Nat. Gas Sci. Eng.* **2014**, *21*, 874−885.

(3) Yang, Y.; Liu, S. M. Review of shale gas sorption and its models. *Energy Fuels* **2020**, *34*, 15502−15524.

(4) Zhou, S. W.; Wang, H. Y.; Li, B. B.; Li, S. S.; Sepehrnoori, K.; Cai, J. C. Predicting adsorbed gas capacity of deep shales under high temperature and pressure: Experiments and modelling. *Adv. Geo-Energy Res.* **2022**, *6* (6), 482−491.

(5) Liang, H. B.; Qi, Z. L.; Wang, S.; Huang, X. L.; Yan, W. D.; Yuan, Y. Z.; Li, Z. Q. Adsorption models for shale gas: A mini-review. *Energy Fuels* **2022**, *36*, 12946−12960.

(6) Gao, Q.; Liu, J. S.; Huang, Y. F.; Li, W.; Shi, R.; Leong, Y. K.; Elsworth, D. A critical review of coal permeability models. *Fuel* **2022**, *326*, 125124.

(7) Schwartz, B.; Elsworth, D. Sorptive permeability loss determined from strain-based analysis of tightly constrained experiments on shale. *J. Petrol. Sci. Eng.* **2022**, *214*, 110502.

(8) Gao, Q.; Cheng, Y. F.; Han, S. C.; Yan, C. L.; Li, Y.; Han, Z. Y. Effect of shale matrix heterogeneity on gas transport during production: A microscopic investigation. *J. Petrol. Sci. Eng.* **2021**, *201*, 108526.

(9) Pang, Y.; Chen, S. N.; Soliman, M. Y.; Morse, S. M.; Hu, X. F. Evaluation of matrix swelling behavior in shale induced by methane sorption under triaxial stress and strain conditions. *Energy Fuels* **2019**, *33*, 4986−5000.

(10) Javadpour, F. Nanopores and Apparent Permeability of Gas Flow in Mudrocks (Shales and Siltstone). *J. Can. Petrol. Technol.* **2009**, *48* (08), 16−21.

(11) Zeng, J.; Liu, J. S.; Li, W.; Leong, Y. K.; Elsworth, D.; Guo, J. C. Shale gas reservoir modeling and production evaluation considering complex gas transport mechanisms and dispersed distribution of kerogen. *Petrol. Sci.* **2021**, *18*, 195−218.

(12) Liu, X. Y.; Zhang, L. H.; Zhao, Y. L.; He, M.; Wu, J. F.; Su, S. W. Shale gas transport in nanopores: Contribution of different transport mechanisms and influencing factors. *Energy Fuels* **2021**, *35*, 2033−2047.

(13) Sheng, G. L.; Su, Y. L.; Javadpour, F.; Wang, W. D.; Zhan, S. Y.; Liu, J. H.; Zhong, Z. New slip coefficient model considering adsorbed gas diffusion in shale gas reservoirs. *Energy Fuels* **2020**, *34* (10), 12078−12087.

(14) Fink, R.; Krooss, B. M.; Gensterblum, Y.; Amann-Hildenbrand, A. Apparent permeability of gas shales - Superposition of fluid-dynamic and poro-elastic effects. *Fuel* **2017**, *199*, 532−550.

(15) Zhao, Y.; Wang, C. L.; Zhang, Y. F.; Liu, Q. Experimental study of adsorption effects on shale permeability. *Nat. Resour. Res.* **2019**, *28* (4), 1575−1586.

(16) Letham, E. A. Matrix Permeability Measurements of Gas Shales: Gas Slippage and Adsorption as Sources of Systematic Error. Undergraduate Honours Thesis, University of British Columbia, 2011.

(17) Alnoaimi, K.; Kovscek, A. Experimental and numerical analysis of gas transport in shale including the role of sorption. Presented at the SPE Annual Technical Conference and Exhibition, New Orleans, LA, USA, 2013.

(18) Aljamaan, H.; Alnoaimi, K.; Kovscek, A. R. In-depth experimental investigation of shale physical and transport properties.

(19) Zamirian, M.; Aminian, K. K.; Ameri, S.; Fathi, E. New steady-state technique for measuring shale core plug permeability. Presented at the SPE/CSUR Unconventional Resources Conference-Canada, Calgary, AB, Canada, 2014.

(20) Jin, G.; Perez, H. G.; Agrawal, G.; Khodja, M. R.; Ali, A. Z.; Hussaini, S. R.; Jangda, Z. Z. The impact of gas adsorption and composition on unconventional shale permeability measurement. Presented at the SPE Middle East Oil & Gas Show and Conference, Manama, Bahrain, 2015.

(21) Peng, S.; Loucks, B. Permeability measurements in mudrocks using gas-expansion methods on plug and crushed-rock samples. *Mar. Petrol. Geol.* **2016**, *73*, 299−310.

(22) Nazari Moghaddam, R.; Jamiolahmady, M. Fluid transport in shale gas reservoirs: Simultaneous effects of stress and slippage on matrix permeability. *Int. J. Coal Geol.* **2016**, *163*, 87−99.

(23) Moghadam, A. A.; Chalaturnyk, R. Laboratory Investigation of Shale Permeability. Presented at the SPE/CSUR Unconventional Resources Conference, Calgary, AB, Canada, 2015.

(24) Heller, R.; Vermylen, J.; Zoback, M. Experimental investigation of matrix permeability of gas shales. *AAPG Bull.* **2014**, *98* (5), 975−995.

(25) Firouzi, M.; Alnoaimi, K.; Kovscek, A.; Wilcox, J. Klinkenberg effect on predicting and measuring helium permeability in gas shales. *Int. J. Coal Geol.* **2014**, *123*, 62−68.

(26) Cui, X.; Bustin, R. M.; Brezovski, R.; Nassichuk, B.; Glover, K.; Pathi, V. A new method to simultaneously measure in-situ permeability and porosity under reservoir conditions: implications for characterization of unconventional gas reservoirs. Presented at the Canadian Unconventional Resources and International Petroleum Conference, Calgary, AB, Canada, 2010.

(27) Moghadam, A. A.; Chalaturnyk, R. Analytical and experimental investigations of gas-flow regimes in shales considering the influence of mean effective stress. *SPE J.* **2016**, *21* (02), 557−572.

(28) Gao, J.; Yu, Q. C. Effect of water saturation on pressure-dependent permeability of carboniferous shale of the qaidam basin, China. *Transport Porous. Med.* **2018**, *123*, 147−172.

(29) Chen, T. Y.; Feng, X. T.; Cui, G. L.; Tan, Y. L.; Pan, Z. J. Experimental study of permeability change of organic-rich gas shales under high effective stress. *J. Nat. Gas Sci. Eng.* **2019**, *64*, 1−14.

(30) Pan, Z. J.; Ma, Y.; Danesh, N. N.; Connell, L. D.; Sander, R.; Down, D. I.; Camilleri, M. Measurement of shale anisotropic permeability and its impact on shale gas production. Presented at the SPE Asia Pacific Unconventional Resources Conference and Exhibition, Brisbane, Australia, 2015.

(31) Zhou, J. P.; Liu, G. J.; Jiang, Y. D.; Xian, X. F.; Liu, Q. L.; Zhang, D. C.; Tan, J. Q. Supercritical carbon dioxide fracturing in shale and the coupled effects on the permeability of fractured shale: An experimental study. *J. Nat. Gas Sci. Eng.* **2016**, *36*, 369−377.

(32) Ghanizadeh, A.; Amann-Hildenbrand, A.; Gasparik, M.; Gensterblum, Y.; Krooss, B. M.; Littke, R. Experimental study of fluid transport processes in the matrix system of the European organic-rich shales: II. Posidonia Shale (Lower Toarcian, northern Germany). *Int. J. Coal Geol.* **2014**, *123*, 20−33.

(33) Tan, Y. L.; Pan, Z. J.; Liu, J. S.; Feng, X. T.; Connell, L. D. Laboratory study of proppant on shale fracture permeability and compressibility. *Fuel* **2018**, *222*, 83−97.

(34) Tan, Y. L.; Pan, Z. J.; Liu, J. S.; Wu, Y. T.; Haque, A.; Connell, L. D. Experimental study of permeability and its anisotropy for shale fracture supported with proppant. *J. Nat. Gas Sci. Eng.* **2017**, *44*, 250−264.

(35) Zhou, J.; Zhang, L. Q.; Li, X.; Pan, Z. J. Experimental and modeling study of the stress-dependent permeability of a single fracture in shale under high effective stress. *Fuel* **2019**, *257*, 116078.

(36) Wang, X. Q.; Zhu, Y. M.; Fu, C. Q. Experimental investigation of the stress-dependent permeability in the Longmaxi Formation shale. *J. Petrol. Sci. Eng.* **2019**, *175*, 932−947.

(37) Chen, Y. F.; Jiang, C. B.; Yin, G. Z.; Wojtanowicz, A. K.; Zhang, D. M. Permeability and effective stress in dipping gas shale formation with bedding—experimental study. *J. Energy Resour.* **2020**, *142* (10), 103002.

(38) Mckernan, R. E.; Rutter, E. H.; Mecklenburgh, J.; Taylor, K. G.; Covey-Crump, S. J. Influence of effective pressure on mudstone matrix permeability: implications for shale gas production. Presented at the SPE/EAGE European Unconventional Resources Conference and Exhibition, Vienna, Austria, 2014.

(39) Ma, Y.; Pan, Z. J.; Zhong, N. N.; Connell, L. D.; Down, D. I.; Lin, W. L.; Zhang, Y. Experimental study of anisotropic gas permeability and its relationship with fracture structure of Longmaxi Shales, Sichuan Basin, China. *Fuel* **2016**, *180*, 106−115.

(40) van Noort, R.; Yarushina, V. Water, CO_2 and Argon permeabilities of intact and fractured shale cores under stress. *Rock Mech. Rock Eng.* **2019**, *52*, 299−319.

(41) Li, X.; Feng, Z. J.; Han, G.; Elsworth, D.; Marone, C.; Saffer, D.; Cheon, D. S. Permeability evolution of propped artificial fractures in green river shale. *Rock Mech. Rock Eng.* **2017**, *50*, 1473−1485.

(42) Kumar, H.; Elsworth, D.; Mathews, J. P.; Marone, C. Permeability evolution in sorbing media: analogies between organic-rich shale and coal. *Geofluids* **2016**, *16*, 43−55.

(43) Kang, Y. L.; Chen, M. J.; Li, X. C.; You, L. J.; Yang, B. Laboratory measurement and interpretation of nonlinear gas flow in shale. *Int. J. Mod. Phys. C* **2015**, *26* (06), 1550063.

(44) Ren, Y.; Guo, X.; Xie, C.; Wu, H. Q. Experimental study on gas slippage of Marine Shale in Southern China. *Petroleum* **2016**, *2* (2), 171−176.

(45) Zhu, W. Y.; Tian, W.; Gao, Y.; Deng, J.; Zhang, X. L.; Qi, Q.; Ma, Q. Study on experiment conditions of marine shale gas seepage law. *J. Nat. Gas Geosci.* **2016**, *1* (2), 157−163.

(46) Shen, Y. H.; Pang, Y.; Shen, Z. Q.; Tian, Y. Y.; Ge, H. K. Multiparameter analysis of gas transport phenomena in shale gas reservoirs: apparent permeability characterization. *Sci. Rep.* **2018**, *8* (1), 2601.

(47) Wu, T.; Pan, Z. J.; Connell, L. D.; Camilleri, M.; Fu, X. F. Apparent gas permeability behaviour in the near critical region for real gases. *J. Nat. Gas Sci. Eng.* **2020**, *77*, 103245.

(48) Klinkenberg, L. The permeability of porous media to liquids and gases. In *API Drilling and Production Practice*; American Petroleum Institute: 1941; pp 200−213.

(49) Beskok, A.; Karniadakis, G. E. Report: a model for flows in channels, pipes, and ducts at micro and nano scales. *Microsc. Therm. Eng.* **1999**, *3*, 43−77.

(50) Florence, F. A.; Rushing, J. A.; Newsham, K. E.; Blasingame, T. A. Improved permeability prediction relations for low permeability sands. Presented at the Rocky Mountain Oil & Gas Technology Symposium, Denver, CO, USA, 2007.

(51) Civan, F.; Rai, C. S.; Sondergeld, C. H. Shale-gas permeability and diffusivity inferred by improved formulation of relevant retention and transport mechanisms. *Transport Porous. Med.* **2011**, *86*, 925−944.

(52) Freeman, C. M.; Moridis, G. J.; Blasingame, T. A. A numerical study of microscale flow behavior in tight gas and shale gas reservoir systems. *Transport Porous. Med.* **2011**, *90*, 253−268.

(53) Darabi, H.; Ettehad, A.; Javadpour, F.; Sepehrnoori, K. Gas flow in ultra-tight shale strata. *J. Fluid Mech.* **2012**, *710*, 641−658.

(54) Naraghi, M. E.; Javadpour, F. A stochastic permeability model for the shale-gas systems. *Int. J. Coal Geol.* **2015**, *140*, 111−124.

(55) Wu, K. L.; Li, X. F.; Guo, C. H.; Wang, C. C.; Chen, Z. X. A unified model for gas transfer in nanopores of shale-gas reservoirs: coupling pore diffusion and surface diffusion. *SPE J.* **2016**, *21*, 1583−1611.

(56) Wu, K. L.; Li, X. F.; Wang, C. C.; Chen, Z. X.; Yu, W. A model for gas transport in microfractures of shale and tight gas reservoirs. *AIChE J.* **2015**, *61* (6), 2079−2088.

(57) Wang, S.; Shi, J. T.; Wang, K.; Sun, Z.; Miao, Y. N.; Hou, C. H. Apparent permeability model for gas transport in shale reservoirs with nanoscale porous media. *J. Nat. Gas Sci. Eng.* **2018**, *55*, 508−519.

(58) Sheng, G. L.; Su, Y. L.; Zhao, H.; Liu, J. H. A unified apparent porosity/permeability model of organic porous media: Coupling complex pore structure and multi-migration mechanism. *Adv. Geo-Energy Res.* **2020**, *4* (2), 115−125.

(59) Wang, X. K.; Sheng, J. Gas sorption and non-Darcy flow in shale reservoirs. *Petrol. Sci.* **2017**, *14*, 746−754.

(60) Wang, S.; Shi, J. T.; Wang, K.; Sun, Z.; Zhao, Z. F. New coupled apparent permeability models for gas transport in inorganic nanopores of shale reservoirs considering multiple effects. *Energy Fuels* **2017**, *31*, 13545−13557.

(61) Wang, T. Y.; Tian, S. C.; Zhang, W. H.; Ren, W. X.; Li, G. S. Production model of a fractured horizontal well in shale gas reservoirs. *Energy Fuels* **2021**, *35*, 493−500.

(62) Mu, Z. Q.; Ning, Z. F.; Gu, K. M.; Lyu, F. T. Apparent permeability coupling of adsorbed and free gases for deep shale: theoretical model and measurements. *Energy Fuels* **2022**, *36*, 11849−11860.

(63) Hatami, M.; Bayless, D.; Sarvestani, A. A model for stress-dependence of apparent permeability in nanopores of shale gas reservoirs. *AIChE J.* **2020**, *66* (10), e16541.

(64) Li, Y.; Dong, P. C.; Li, W. R.; Mi, L. D.; Yang, S.; Cao, N.; Yi, X. Y. The gas flow in micro fractures of shale gas reservoirs. Presented at the SPE Middle East Oil & Gas Show and Conference, Manama, Kingdom of Bahrain, 2017.

(65) Song, W. H.; Yao, J.; Li, Y.; Sun, H.; Zhang, L.; Yang, Y. F.; Zhao, J. L.; Sui, H. G. Apparent gas permeability in an organic-rich shale reservoir. *Fuel* **2016**, *181*, 973−984.

(66) Wang, H. Y.; Marongiu-Porcu, M. Impact of Shale-gas apparent permeability on production: combined effects of non-darcy flow/gas slippage, desorption, and geomechanics. *SPE Reserv. Eval. Eng.* **2015**, *18* (04), 495−507.

(67) Cao, P.; Liu, J. S.; Leong, Y. K. General gas permeability model for porous media: bridging the gaps between conventional and unconventional natural gas reservoirs. *Energy Fuels* **2016**, *30*, 5492−5505.

(68) Wang, H. Y. What factors control shale-gas production and production-decline trend in fractured systems: a comprehensive analysis and investigation. *SPE J.* **2017**, *22* (02), 562−581.

(69) Abolghasemi, E.; Andersen, P.Ø. The influence of adsorption layer thickness and pore geometry on gas production from tight compressible shales. *Adv. Geo-Energy Res.* **2022**, *6* (1), 4−22.

(70) Cao, P.; Liu, J. S.; Leong, Y. K. Combined impact of flow regimes and effective stress on the evolution of shale apparent permeability. *Journal of Unconventional Oil and Gas Resources* **2016**, *14*, 32−43.

(71) Wei, M. Y.; Liu, J. S.; Feng, X. T.; Wang, C. G.; Zhou, F. B. Evolution of shale apparent permeability from stress-controlled to displacement-controlled conditions. *J. Nat. Gas Sci. Eng.* **2016**, *34*, 1453−1460.

(72) Wang, Y.; Liu, S. M.; Zhao, Y. X. Modeling of permeability for ultra-tight coal and shale matrix: A multimechanistic flow approach. *Fuel* **2018**, *232*, 60−70.

(73) Shi, R.; Liu, J. S.; Wang, X. M.; Wei, M. Y.; Elsworth, D. A critical analysis of shale laboratory permeability evolution data. *Energy* **2021**, *236*, 121405.

(74) Peng, Y.; Liu, J. S.; Pan, Z. J.; Qu, H. Y.; Connell, L. D. Evolution of shale apparent permeability under variable boundary conditions. *Fuel* **2018**, *215*, 46−56.

(75) Yang, X.; Zhang, H. B.; Wu, W. B.; Gong, Z. H.; Yuan, W. F.; Feng, X. Q.; Gu, B. Gas migration in the reservoirs of ultra-low porosity and permeability based on an improved apparent permeability model. *J. Petrol. Sci. Eng.* **2020**, *185*, 106614.

(76) Ying, Q.; Zhang, H. B.; Zhao, J.; Wu, W. B.; Gu, B.; Feng, X. Q. Influence of considering the sorption effect in the betti-maxwell reciprocal theorem on gas transport capacity in unconventional reservoirs. *Transport Porous. Med.* **2021**, *137*, 451−469.

(77) Li, Y. D.; Dong, P. C.; Zhou, D. W. A dynamic apparent permeability model for shale microfractures: Coupling porome-

chanics, fluid dynamics, and sorption-induced strain. *J. Nat. Gas Sci. Eng.* **2020**, *74*, 103104.

(78) Li, W. R.; Ju, Y.; Zhou, H. W.; Wang, K. Novel shale permeability model coupling sorption-induced differential deformation and multiple flow regimes. *Energy Fuels* **2022**, *36* (19), 11777−11786.

(79) Gao, Q.; Han, S. C.; Cheng, Y. F.; Li, Y.; Yan, C. L.; Han, Z. Y. Apparent permeability model for gas transport through micropores and microfractures in shale reservoirs. *Fuel* **2021**, *285*, 119086.

(80) Zeng, F. H.; Peng, F.; Guo, J. C.; Rui, Z. H.; Xiang, J. H. Gas mass transport model for microfractures considering the dynamic variation of width in shale reservoirs. *SPE Reserv. Eval. Eng.* **2019**, *22* (04), 1265−1281.

(81) Xie, J. Q.; Xiong, W.; Tan, Y. L.; Cui, G. L.; Pan, H. Z.; Sun, Z. H. Effects of anisotropic permeability evolution on shale gas production: an internal swelling factor model. *Energy Fuels* **2022**, *36* (2), 771−785.

(82) Cai, J. C.; Lin, D. L.; Singh, H.; Wei, W.; Zhou, S. W. Shale gas transport model in 3D fractal porous media with variable pore sizes. *Mar. Petrol. Geol.* **2018**, *98*, 437−447.

(83) Sun, Z. H.; Chen, T. Y.; Zhu, L. H.; Lu, J. Y.; Zhang, S. J.; Pan, Z. J.; Cui, G. L. Analysis of the upper and lower boundaries of permeability evolution during shale rock shear deformation. *Energy Fuels* **2022**, *36*, 2007−2022.

(84) Shi, R.; Liu, J. S.; Wei, M. Y.; Elsworth, D.; Wang, X. M. Mechanistic analysis of coal permeability evolution data under stress-controlled conditions. *Int. J. Rock Mech. Min.* **2018**, *110*, 36−47.

(85) Du, X. D.; Gu, M.; Liu, Z. J.; Zhao, Y.; Sun, F. L.; Wu, T. F. Enhanced shale gas recovery by the injections of CO_2, N_2, and CO_2/N_2 mixture gases. *Energy Fuels* **2019**, *33*, 5091−5101.

(86) Cao, P.; Liu, J. S.; Leong, Y. K. A fully coupled multiscale shale deformation-gas transport model for the evaluation of shale gas extraction. *Fuel* **2016**, *178*, 103−117.

(87) Zeng, J.; Liu, J. S.; Guo, J. C. Characterization of gas transport in shale: A multi-mechanism permeability modeling approach. *Chem. Eng. J.* **2022**, *438*, 135604.

(88) Javadpour, F.; Singh, H.; Rabbani, A.; Babaei, M.; Enayati, S. Gas flow models of shale: a review. *Energy Fuels* **2021**, *35*, 2999−3010.

(89) Zeng, J.; Liu, J. S.; Li, W.; Leong, Y. K.; Elsworth, D.; Guo, J. C. Evolution of shale permeability under the influence of gas diffusion from the fracture wall into the matrix. *Energy Fuels* **2020**, *34* (4), 4393−4406.

(90) Gao, Q.; Han, S. C.; Cheng, Y. F.; Shi, X.; Yan, C. L.; Han, Z. Y. Flow-coupled-geomechanical modelling of CO_2 transport in depleted shale from a microscopic perspective. *Energy* **2022**, *257*, 124727.

(91) Gao, Q.; Cheng, Y. F.; Han, S. C.; Li, Y.; Yan, C. L.; Han, Z. Y. Coupled hydro-mechanical modeling of gas flow in shale matrix considering the fractal characteristics of nanopores. *Fractals* **2021**, *29* (08), 2150266.

(92) Wei, M. Y.; Liu, Y. K.; Liu, J. S.; Elsworth, D.; Zhou, F. B. Micro-scale investigation on coupling of gas diffusion and mechanical deformation of shale. *J. Petrol. Sci. Eng.* **2019**, *175*, 961−970.

(93) Tian, J. W.; Liu, J. S.; Elsworth, D.; Leong, Y. K.; Li, W.; Zeng, J. Shale gas production from reservoirs with hierarchical multiscale structural heterogeneities. *J. Petrol. Sci. Eng.* **2022**, *208*, 109380.

(94) Li, W.; Liu, J. S.; Zeng, J.; Leong, Y. K.; Elsworth, D.; Tian, J. W.; Li, L. A fully coupled multidomain and multiphysics model for evaluation of shale gas extraction. *Fuel* **2020**, *278*, 118214.

(95) Yan, C.; Li, Y.; Cheng, Y.; Wei, J.; Tian, W.; Li, S.; Wang, Z. Multifield coupling mechanism in formations around a wellbore during the exploitation of methane hydrate with CO_2 replacement. *Energy* **2022**, *245*, 123283.

(96) Tian, J. W.; Liu, J. S.; Elsworth, D.; Leong, Y. K.; Li, W. Linking fractal theory to a fully coupled coal deformation and two-phase flow multiphysics: The role of fractal dimensions. *Energy Fuels* **2022**, *36*, 12591−12605.

(97) Harpalani, S.; Chen, G. Estimation of changes in fracture porosity of coal with gas emission. *Fuel* **1995**, *74*, 1491−1498.

(98) Cui, X. J.; Bustin, R. M. Volumetric strain associated with methane desorption and its impact on coalbed gas production from deep coal seams. *AAPG Bull.* **2005**, *89* (9), 1181−1202.

(99) Zhang, H. B.; Liu, J. S.; Elsworth, D. How sorption-induced matrix deformation affects gas flow in coal seams: A new FE model. *Int. J. Rock Mech. Min.* **2008**, *45*, 1226−1236.

(100) Shi, R.; Liu, J. S.; Wang, X. M.; Elsworth, D.; Wang, Z. Z.; Wei, M. Y.; Cui, G. L. Experimental observations of gas-sorption-induced strain gradients and their implications on permeability evolution of shale. *Rock Mech. Rock Eng.* **2021**, *54*, 3927−3943.

(101) Shi, R.; Liu, J. S.; Wang, X. M.; Elsworth, D.; Liu, Z. H.; Wei, M. Y.; Liu, X. X.; Wang, Z. Z. Experimental observations of heterogeneous strains inside a dual porosity sample under the influence of gas-sorption: A case study of fractured coal. *Int. J. Coal Geol.* **2020**, *223*, 103450.

(102) Connell, L. D.; Lu, M.; Pan, Z. J. An analytical coal permeability model for tri-axial strain and stress conditions. *Int. J. Coal Geol.* **2010**, *84*, 103−114.

(103) Liu, H. H.; Rutqvist, J. A new coal-permeability model: internal swelling stress and fracture-matrix interaction. *Transport Porous. Med.* **2010**, *82*, 157−171.

(104) Jiang, C. Z.; Zhao, Z. F.; Zhang, X. W.; Liu, J. S.; Elsworth, D.; Cui, G. L. Controlling effects of differential swelling index on evolution of coal permeability. *J. Rock Mech. Geotech.* **2020**, *12*, 461−472.

(105) Jia, C. Q.; Huang, Z. Q.; Sepehrnoori, K.; Yao, J. Modification of two-scale continuum model and numerical studies for carbonate matrix acidizing. *J. Petrol. Sci. Eng.* **2021**, *197*, 107972.

⊕ Recommended by ACS

Effect of Acid Type on Acid-Etched Fracture Surface Morphology and Conductivity along the Fracture

Bo Gou, Qian Dai, *et al.*

FEBRUARY 09, 2023
ENERGY & FUELS   READ ⬈

An Apparent Permeability Model in Organic Shales: Coupling Multiple Flow Mechanisms and Factors

Haosheng Song, Yunna Ding, *et al.*

MARCH 06, 2023
LANGMUIR   READ ⬈

Relationship between Shale Hydration and Shale Collapse

Wenxin Dong, Deyi Jiang, *et al.*

NOVEMBER 11, 2022
ACS OMEGA   READ ⬈

Fractal Apparent Permeability Model for Coal under the Coupling Actions of Stress and Water

Shulei Duan, Yunna Ding, *et al.*

MARCH 13, 2023
ENERGY & FUELS   READ ⬈

Get More Suggestions >